Steel and Composite Structures, *Vol. 29, No. 2 (2018) 161-173*
DOI: https://doi.org/10.12989/scs.2018.29.2.161

Finite element modeling of rolled steel shapes subjected to weak axis bending

Najib G. Saliba *1, Issam Tawk [2] and Antoine N. Gergess [1]

[1] *Department of Civil Engineering, University of Balamand, El-Koura, Lebanon*
[2] *Department of Mechanical Engineering, University of Balamand, El-Koura, Lebanon*

(*Received February 8, 2018, Revised July 25, 2018, Accepted August 24, 2018*)

Abstract. Point bending is often used for cambering and curving structural steel girders. An analytical solution, applicable in the elasto-plastic range only, that relates applied loads to the desired curve was recently developed for inducing horizontal curves using four-point bending. This solution does not account for initial residual stresses and geometric imperfections built-in hot-rolled sections. This paper presents results from a full-scale test on a hot-rolled steel section curved using four-point bending. In parallel, a numerical analysis, accounting for both initial geometric imperfections and initial residual stresses, was carried out. The models were validated against the experimental results and a good agreement for lateral offset and for strain in the elasto-plastic and post-plastic ranges was achieved. The results show that the effect of initial residual stresses on deformation and strain is minimal. Finally, residual stresses due to cold bending calculated from the numerical analysis were assessed and a revised stress value for the service load design of the curved girder is proposed.

Keywords: curving; elasto-plastic; finite element; non-linear; point bending; post-plastic; residual stress; steel

1. Introduction

Four-point bending is sometimes used to induce horizontal and vertical curves in structural steel girders (Gergess and Sen 2010, 2016). In this process, the straight fabricated girder is bent by two equidistant loads applied approximately at the third points using hydraulic jacks. The curved profile develops from permanent residual deformation induced upon removing the loads. The resulting curve is not circular but closer to a parabolic shape. An analytical solution was recently presented (Gergess and Sen 2016) to evaluate the geometric shapes induced by point bending and explore loading configurations that better approximate circular curves. Accuracy and applicability of the analytical solution was verified by comparing predictions against available experimental results from a full-scale test (Fig. 1). Reasonable correlation was obtained with experimental results (Gergess and Sen 2016), however, comparisons were limited to the elasto-plastic range and couldn’t account for plastic and post-plastic loads. Moreover, the effects of initial residual stress and girder initial geometric imperfection that are evident in hot-rolled sections were not considered.

The initial section of this paper presents a brief description of the full-scale testing and results were used to validate a numerical modelling that was carried out in the subsequent sections. The finite element package ABAQUS was used for this purpose as it allows monitoring the girder deformed geometry in the elasto-plastic and post-plastic ranges. The exact stress-strain curve of steel idealizing the “plastic” and “strain hardened” region was incorporated in the model (Fig. 2). Note that the girder under study is made of Grade 275 with a measured yield stress of 290.7 MPa. Preliminary results show good agreement with measured strain and deformation.

Following the validation of the finite element model, the effects of initial geometric imperfection and initial residual stress on the girder response were investigated. Finally, results from increasing the point bending load into the post-plastic range were included. It is shown that residual stresses that build up from point bending directly affect the structural performance of the steel girder in service (Keating and Christian 2009) and exceed current code values. Consequently, more conservative values are recommended for future use.

Fig. 1 Full-scale test girder set-up

∗Corresponding author, Associate Professor,
E-mail: najib.saliba@balamand.edu.lb

http://www.techno-press.org/?journal=scs&subpage=6 ISSN: 1229-9367 (Print), 1598-6233 (Online)

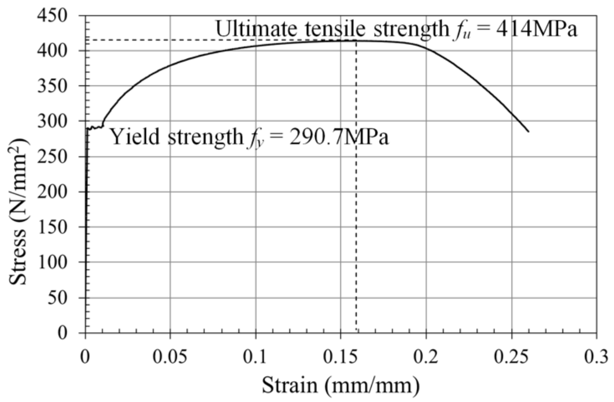

Fig. 2 Stress-strain curve for the IPE600 carbon steel based on measurement

2. Objectives

The overall goal of the study is to conduct an in-depth investigation of the structural behaviour of hot-rolled steel sections bent about their weak axis using four-point bending. The principal objectives are:

(1) Develop and validate a three-dimensional, non-linear model for four-point bending using results from a full-scale test girder.
(2) Account for initial geometric imperfections and residual stress. Although it is anticipated that their effects on the response of the steel girder subjected to the same point-bending configuration is minimal they are considered for completeness.
(3) Examine the steel girder response in the post-plastic range by increasing the magnitude of the point bending loads.
(4) Determine and assess the effects of residual stresses that build up from point bending.

3. Experimental study

A synopsis of the key features of the full-scale test used to validate the finite element model is presented.

3.1 Model details

The tested steel girder is an IPE600 European section (relatively similar to a W610×215 according to the American Institute of Steel Construction (AISC) (ANSI/AISC 360-10 2015)). The girder basic geometry was carefully measured prior to testing: the total length of the beam L' is 5950 mm (Fig. 3(a)), its flange width and thickness are 220 mm and 19 mm respectively, and the web depth and thickness are 600 mm and 12 mm (Fig. 3(b)).

3.2 Material testing

Prior to performing the four-point bending operation, a tensile strength test was carried out for three coupons extracted from the web of the structural steel hot rolled section. The three coupons were flat with specimen dimensions of 71×8.25×12 mm (length × width × thickness) and were tested in accordance with ASTM E8/E8M-13a (ASTM 2014) using a YL-15 UTM machine with a strain rate of 0.001 per second. The actual yield stress was measured as f_y = 290.7 MPa (larger than the nominal value of 275 MPa provided by the manufacturer), the corresponding yield strain ε_y = 1385 $\mu\varepsilon$ and the elastic modulus of elasticity E = 210 GPa. The ultimate tensile strength was measured as f_u = 414 MPa. The stress-strain curve adopted in this study based on measurements is presented in Fig. 2. These results were incorporated in the finite element analysis to replicate the real characteristics of the material under study (discussed in details in Section 4.1.2).

3.3 Four-point bending test

The girder rested horizontally (weak axis bending) on end rolling supports placed 220 mm inwards from its ends, hence the distance between the supports was L = 5510 mm (Fig. 3(a)). The end supports allow horizontal displacement and rotation (Fig. 4(a)). The loads were applied to the girder at two points spaced 2200 mm apart (or at 1655 mm measured from the supporting ends of the girder, Fig. 3(a)) using a steel frame mounted horizontally and connected to the vertical hydraulic jack of a 100 tonne UTM machine (Fig. 1). Steel load distribution plates were utilised at the

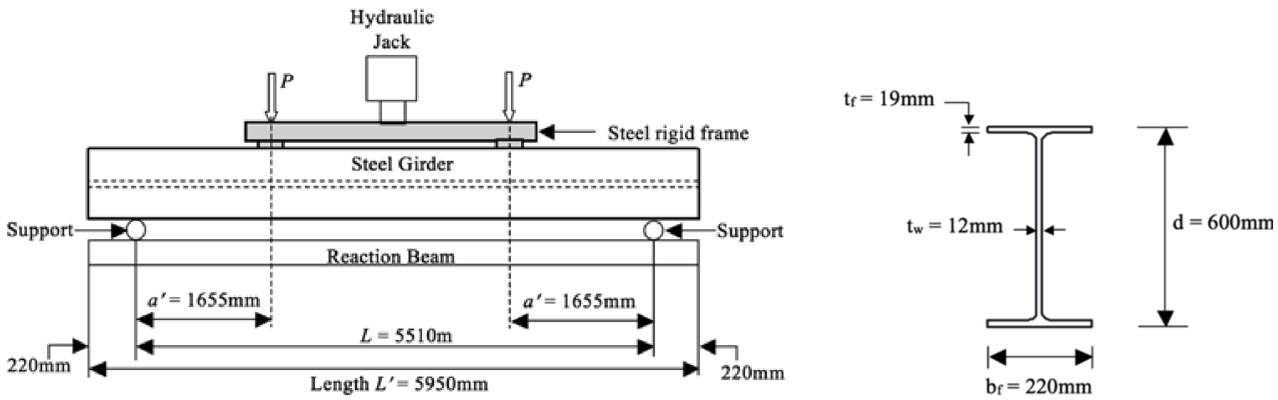

(a) Girder layout during four-point bending (b) Girder cross-section

Fig. 3 Structural steel girder layout and details location of the point loads to avoid localised damage to the flanges (Fig. 4(b)).

The total maximum load applied to the girder was 163 kN (i.e. P = 81.5 kN at each load location, Fig. 3(a)). Prior to reaching this maximum load, the girder was unloaded when it reached a total bending load of 157 kN (P = 78.5 kN) and measurements were recorded during loading and unloading. Note that the 157 kN total load corresponds to the elasto-plastic range (immediately before the section becomes fully plastic) while the 163 kN presents a post-plastic behaviour (as shown later). The deformed shape at the maximum load of 163 kN is shown in Fig. 1.

Deformation and strain measurements were recorded at different points along the girder length. Strain gauges were attached at 44 different locations alternating between the inner and outer faces of the flanges to monitor strain variation during testing. Six Linear Variable Displacement Transducers (LVDTs) were also distributed along the girder length to measure displacements. Typical strain gauges and LVDTs are shown in Fig. 4(a). The locations of the LVDTs

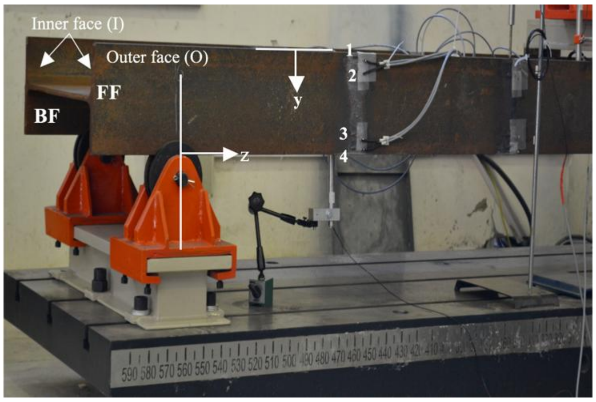

(a) End supports (FF: Front flange, BF: back flange), strain gauges and LVDTs

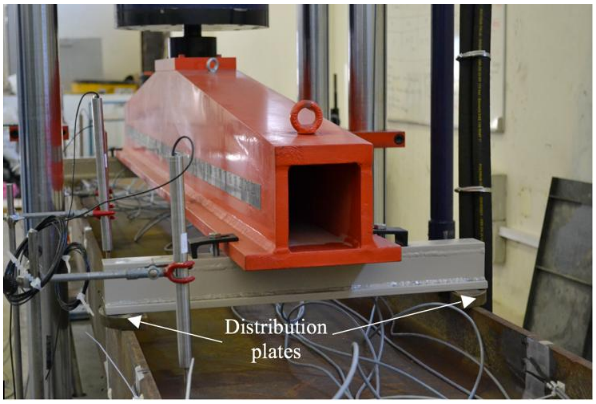

(b) Loading frame and distribution plates

Fig. 4 Test set-up

Table 1 Strain gauge locations

Designation	z (cm)	y (cm)	Designation	z (cm)	y (cm)
A1 FF	55.5	1.0	A1 BFO	55.5	1.0
A2 FF*	55.55	4.0	A2 BFO	55.5	4.0
A3 FF	55.5	17.8	A3 BFO	55.5	17.8
A4 FF	55.5	20.7	**A4 BFO***	55.5	20.6
B1 FF*	99.5	1.2	B1 BFI	109.7	1.2
B2 FF	99.5	4.2	**B2 BFI***	109.7	4.1
B3 FF	99.5	17.6	B3 BFO	108.8	17.8
B4 FF	99.5	20.7	B4 BFO	108.8	20.6
C1 FF	165.0	1.4	C1 BFI	166.3	4.2
C2 FF	165.0	4.3	C2 BFI	166.3	4.3
C3 FF*	165.0	18.0	C3 BFO	164.5	17.7
C4 FF	165.0	20.6	**C4 BFO***	164.5	20.4
D1 FF*	275.0	1.0	D1 BFI	276.0	1.4
D2 FF	275.0	4.0	**D2 BFI***	276.0	5.0
D3 FF*	275.0	17.8	D3 BFO	276.3	17.6
D4 FF	275.0	20.8	**D4 BFO***	276.3	20.3
E1 FF*	351.0	1.2	**F1 BFI***	412.5	1.3
E2 FF*	351.0	4.3	F2 BFI	412.5	4.6
E3 FF*	351.5	17.9	**F3 BFO***	413.0	17.8
E4 FF	411.7	1.2	F4 BFO	413.0	20.7
F1 FF*	411.7	1.2			
F2 FF	411.7	4.1			

*Critical locations where measurements were used for comparisons

*Note on designation:

first term shows the location horizontally (A to F, Fig. 5); second term shows the location vertically (1 to 4, Fig. 4(a)); the third and fourth terms designate the Front Flange (FF) or the back flange (BF), Fig. 4(a); the last term designates the Inside Face (I) or the Outside Face (O), (Fig. 4(a))

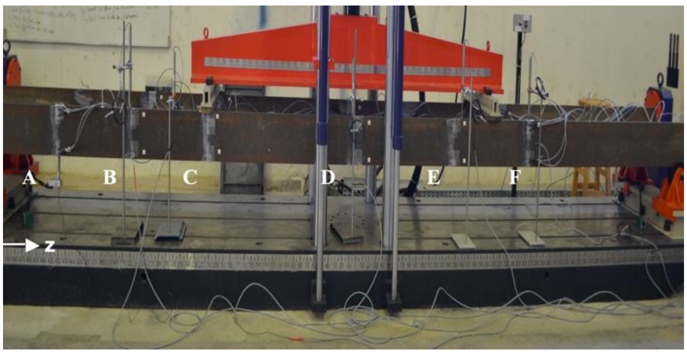

Fig. 5 Strain gauge and LDVTs locations (BF: back flange, FF: front flange)

Table 2 LDVTs Location (Fig. 5)

Designation	A	B	C	D	E	F
z (cm)	55	110	140	275	360	415

and strain gauges are shown in Fig. 5. Four strain gauges were placed along the flange width at each location (Fig. 4(a)) alternating between the inner and outer faces of the two flanges. Locations are labelled as A to F in Fig. 5 and are measured with respect to the left end support (distance z, Figs. 4(a) and 5). The flanges are labelled FF for the front flange and BF for the back flange as shown in Fig. 4(a). The outside face of each flange is labelled O and the inside face I (Fig. 4(a)). The location of each strain gauge is shown in Table 1, measured vertically from the top flange (distance y, Fig. 4(a)). LVDTs were placed at 6 different points along the girder length as provided in Table 2.

Point loads and corresponding displacement and strain were recorded at one-second intervals using the data acquisitions system FDS DAQ. As mentioned earlier, the girder was first loaded to a total bending load of 157 kN, unloaded, reloaded to 163 kN and then unloaded.

4. Numerical study

4.1 Modelling details

The numerical solution relied on the general-purpose finite element analysis package ABAQUS (Hibbitt *et al*. 2012). Results obtained from the experiment were used to validate the finite element model. A detailed description of the numerical modelling carried out in this study is presented herein.

The numerical solution relied on the general-purpose finite element analysis package ABAQUS (Hibbitt *et al*. 2012). Results obtained from the experiment were used to validate the finite element model.

4.1.1 Mesh

The general-purpose shell element (referred to as S4R in ABAQUS mesh element library, (Hibbitt *et al*. 2012)) is employed to discretize the finite element model. It is a four-node doubly curved element with reduced integration and finite membrane strains. This element is widely used in the industry as it is suitable for various shell thickness, it is computationally efficient compared to other mesh elements and has been employed successfully on similar structural steel members (Saliba and Gardner 2013, Thombare *et al*. 2016, Wang *et al*. 2016).

The element size adopted in this study is 15 mm × 15 mm (fine mesh), selected after carrying out a mesh sensitivity analysis in the elastic range. The generated mesh comprises a total of 26,522 elements and 27,404 nodes with 15,086 elements in the web, 5,558 elements in each flange and 160 elements in each load distribution plate (Fig. 4(b)). The finite element mesh is shown in Fig. 6.

4.1.2 Material properties

The stress-strain curve of the steel girder in Fig. 2 was

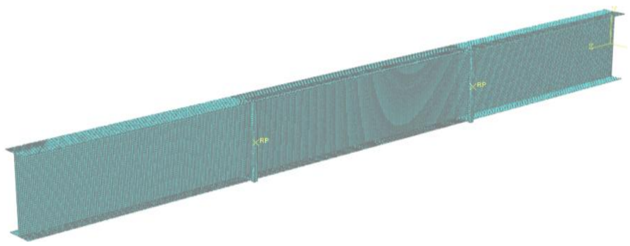

Fig. 6 The finite element model: mesh and bearing plates

obtained from tensile strength coupon test based on the original cross-sectional area without accounting for changes in the cross-section during loading. Measured values correspond to the engineering stress and engineering strain labelled as (σ_{nom}) and (ε_{nom}), respectively. In the finite element model, the stress-strain response was approximated with a multi-linear model defined in terms of the true stress (σ_{true}) and log plastic strain (ε_{ln}^{pl}). The true stress and strain measurement account for actual changes in the cross-sectional area of the tested coupon, whereas those obtained from traditional tensile tests (i.e., σ_{nom}, and ε_{nom}) are measured based on the original cross-sectional area (Chen *et al*. 2016). Relationships between true stress and engineering stress, and log plastic strain and engineering strain, are given by Eqs. (1) and (2) (Wang *et al*. 2017), respectively

$$\sigma_{true} = \sigma_{nom}\,(1 + \varepsilon_{nom}) \qquad (1)$$

$$\varepsilon_{ln}^{pl} = \ln(1+\varepsilon_{nom}) - \frac{\sigma_{true}}{E} \qquad (1)$$

4.1.3 Boundary conditions and load application

The geometry of the tested I-section was replicated in the finite element model based on measurements in the laboratory. Furthermore, boundary conditions were carefully selected to represent the experimental setup. The end supports of the tested girder consisted of rollers that prevented vertical and lateral movements (Fig. 4(a)). Hence, in the finite element model (Fig. 6) the displacements along the vertical (y-axis) and lateral (x-direction) directions were restrained at the end supports location. Moreover, rotation about the longitudinal z-axis (Fig. 6) was restrained to ensure lateral stability (Figs. 4(a) and 6). End supports were located at 220 mm from both ends of the steel girder (Fig. 3(a)). The point loads were applied laterally at 0.3 times the overall length of the girder (e.g., 1873 mm from the girder ends, Fig. 3(a)) using two bearing plates to mimic the test setup (Fig. 4(b)).

4.1.4 Initial geometric imperfections

Geometric imperfections are common in structural steel elements (including, but not limited to, hot-rolling) as they surface during the production and fabrication phases (Reis *et al*. 2016). Although their primary effect is on stability and not on the structural response of the steel girder subjected to the same point-bending configuration, they are considered in this paper as literature on the numerical modeling of rolled I-sections subjected to weak axis bending is scarce. To incorporate the initial geometric imperfections into the

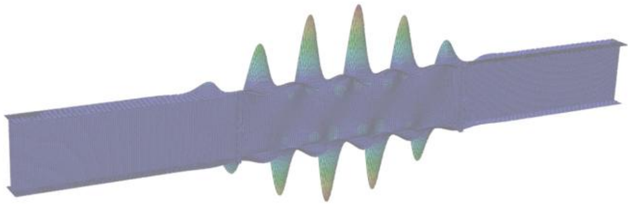

Fig. 7 The initial geometric imperfection mode incorporated in the nonlinear analysis

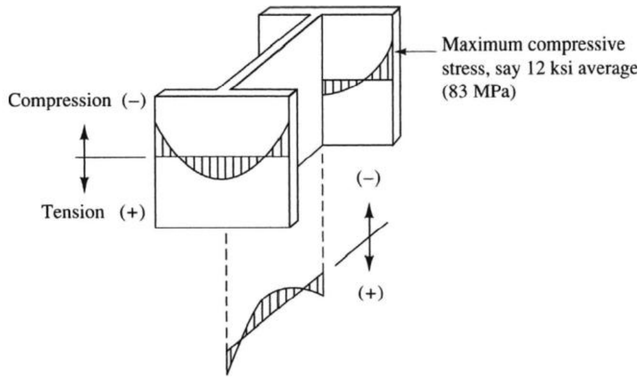

Fig. 8 Initial residual stress pattern in hot-rolled sections (Salmon *et al*. 2010)

finite element model (Hibbitt *et al*. 2012), the analysis had to be performed in two stages. In the first stage, a linear eigenvalue buckling analysis is performed to determine the lowest relevant elastic buckling mode shape of the straight fabricated structure. In the second stage, this mode shape coupled with an imperfection amplitude is input as an initial geometric imperfection for the consequent nonlinear analysis. The selected imperfection mode shape (scale exaggerated) is shown in Fig. 7. It displays the local imperfections at the top and bottom flanges between the load-bearing plates where the point loads were applied (Fig. 4b). Local imperfections in this region where maximum moments and maximum lateral displacements occur are of particular importance. Note that measurements in the laboratory and visual inspection did not reveal global (member) imperfections and therefore only local imperfections were considered.

The nonlinear analysis was carried out using the modified Riks method (Sonck and Belis 2016) (referred to as the Static Riks method in ABAQUS) which is an algorithm that accounts for instabilities that can arise due to geometric imperfections. It can adequately trace nonlinear unloading paths as it adopts an arc-length method to determine the response of the loaded structure (Hibbitt *et al*. 2012).

For the imperfection amplitude, in the absence of local geometric imperfection measurements, four different imperfection amplitudes were considered. The first two imperfection amplitudes were a direct function of the flange thickness (t_f): $t_f/100$ and $t_f/1000$. The third imperfection amplitude was representative of the first simple predictive model (Dawson and Walker 1972): $\omega_{\text{DW1}} = 0.2t_f$. The fourth imperfection amplitude was representative of a more sophisticated predictive model (Dawson and Walker 1972): $\omega_{\text{DW2}} = \gamma(f_y/f_{cr})t_f$ (defined by a coefficient γ multiplied by the ratio of the yield strength f_y to the elastic critical buckling stress σ_{cr}). Dawson and Walker (1972) showed that if coefficient (γ) is set equal to 0.2, reasonable results are obtained.

4.1.5 Initial residual stress

Similar to initial geometric imperfections, residual stresses arise mainly during fabrication without applying external loads and their effects on steel girders subjected to weak axis bending is anticipated to be minimal (considered for completeness of the study). They are self-equilibrating and are usually introduced to structural members when the material deforms into the inelastic region (Keating and Christian 2009, Lay and Ward 1969, Nethercot 1974, Madugula *et al*. 1997). The effect of initial residual stress is to cause premature yielding and loss of stiffness, which can, in certain cases, lead to a substantial worsening in the load carrying capacity of the steel member. Extensive studies have been carried out on initial residual stress in structural carbon steel members and indicated that their magnitude and distribution are highly dependent on the fabrication process. For hot-rolled sections, previous studies (Yun *et al*. 2018, Liu *et al*. 2017, Szalai and Papp 2005) showed that initial residual stress develop mainly due to uneven cooling of the steel section (owed to inconstant thicknesses) and the straightening process that might be used after cooling. Results from these studies also implied that only membrane residual stresses are to be considered due to their noteworthy magnitude while bending residual stresses are minimal and can be ignored.

Several predictive models for the initial residual stress distribution and magnitude are available (Salmon *et al*. 2010, Abambres and Quach 2014). In this paper and in absence of measured values, the predictive model of Salmon *et al*. (2010) for hot-rolled sections was adopted (Fig. 8). This model displays close correlation with the residual stress magnitude by the European Convention for Constructional Steelwork (1984) and the Swedish design code (BSK 99 2003) (developed based on a bi-linear model). Furthermore, the stress distribution is of a parabolic nature as also noted by others (Szalai and Papp 2005, Young 1972, Trahair 1993).

In order to apply the residual stress pattern in Fig. 8, partitions in the top and bottom flanges and the web were created. The relevant stress magnitudes were then input using the "INITIAL CONDITIONS" command in ABAQUS (Hibbitt *et al*. 2012). To equilibrate the residual stress before the application of the point loads, a preliminary load step (known as Static, Linear perturbation in ABAQUS often employed in pre-stressed modal analysis) was initiated (Hibbitt *et al*. 2012).

The residual stress pattern was then modified to show its effect on the girder structural behavior during bending. The magnitude of the residual stress from Fig. 8 was increased by up to 40% and the pattern was modified by changing the dimensions of the stress blocks and switching the stress sign (from compression to tension and vice-versa).

Table 3 Maximum mid-span deformation for P = 78.5 kN considering initial geometric imperfections

Imperfection amplitude	0	$t_f/100$	$t_f/1000$	$\omega_{DW1} = 0.2t_f$	$\omega_{DW2} = \alpha(\sigma_y/\sigma_{cr})t_f$
Deformation from finite element analysis (mm)	118.9	117.0	120.5	115.8	118.2
Measured deformation (mm)	119.4	119.4	119.4	119.4	119.4
Ratio (measured/calculated)	1.004	1.02	0.99	1.031	1.01

4.2 Model validation and discussions

The accuracy of the finite element model was initially evaluated by comparing the results obtained from the experiment to those generated by the software (ABAQUS). The assessment was based on displacement and strain at specific load magnitude. Validation was established for the total load of 157 kN (point load P = 78.5 kN, Fig. 3(a)) considering the four imperfection amplitudes of the initial geometric imperfections discussed in Section 4.4.1. Analysis was first conducted without considering initial residual stress. The effects of initial residual stress (Fig. 8) on the girder behavior during bending were then accounted for.

4.2.1 Effects of initial geometric imperfections

During the experiment, the maximum deformation at midspan for P = 78.5 kN was measured as 119.4 mm. Results from the finite element model show close agreement (difference varies from 1 to 3%) with the experimental results for the four imperfection amplitudes considered. Results for the mid-span displacement are summarized in Table 3.

The imperfection amplitude of $t_f/1000$ was adopted in this paper as it gave the closest value of deformation (120.5 mm compared to 119.4 mm measured, the difference is less than 1%) and comparable results to the more sophisticated predictive model (Dawson and Walker 1972) (120.5 mm compared to 118.2 mm) but is more straightforward to use.

4.2.2 Deformed shapes

The deflected shape of the steel girder based on measured values and finite element results is shown in Fig. 9 at load P = 78.5 kN (total load of 157 kN) and at zero after unloading (residual deformation). The correlation between measured and calculated deformations at load P = 78.5 kN is less than 1% and after unloading less than 3%.

Similar plots are developed in Fig. 10 at P = 81.5 kN (total load of 163 kN) and after unloading. Note that measured deformations at P = 81.5 kN are not included as they exceeded the LVDT's measurement capacity (limited to 150 mm) at locations C, D and E (Fig. 5). Only residual deformations (measured after unloading using a string line stretched between end supports) are shown and the deviation between calculated and measured values varies from 3% at mid-span to 8% at about 0.7 L as shown in Fig. 10.

For completeness, the load-deflection variation based on mid-span numerical and measured deformations is plotted

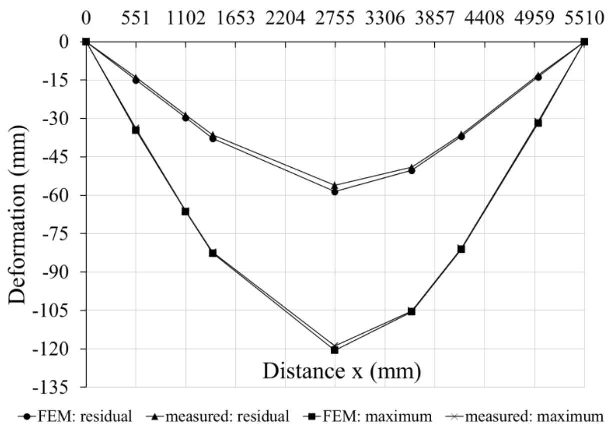

Fig. 9 Deformed shape (FE vs. measured) during loading & unloading P = 78.5 kN

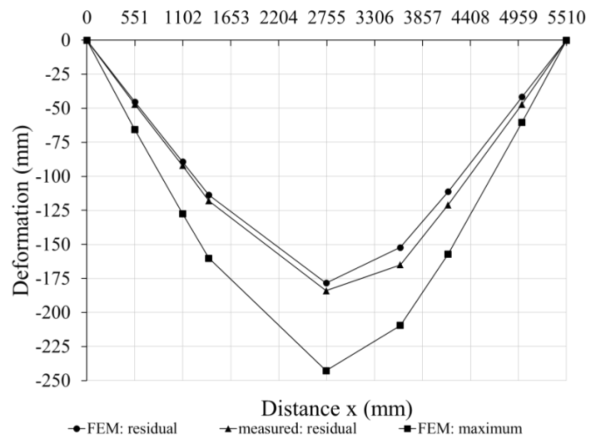

Fig. 10 Deformed shape (FE vs. measured) during loading & unloading P = 81.5 kN

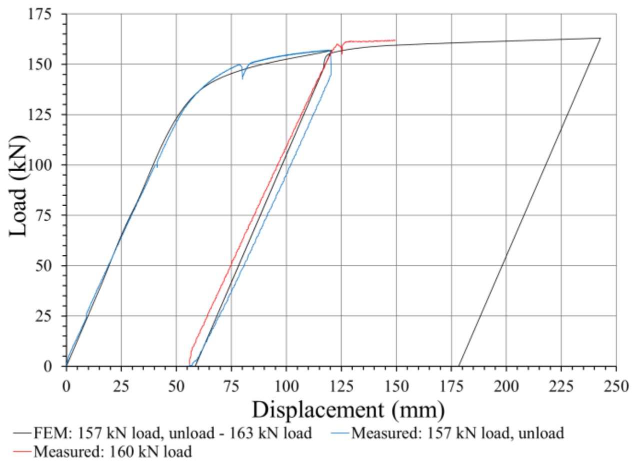

Fig. 11 Load-displacement variation during loading and unloading

in Fig. 11. Plots are shown during loading and unloading from 0 to 157 kN (P = 78.5 kN) and from 0 to 163 kN (P = 81.5 kN). Note that during reloading to 163 kN (P = 81.5 kN), the measured deformations exceeded the limits of the LDVTs (150 mm maximum) after 160 kN (P = 80 kN). Consequently, measured values are shown up to the 160 kN load (P = 80 kN). Only calculated values from the finite element model are shown up to the total load of 163 kN (P = 81.5 kN). Good correlation between measured and calculated values is noted during loading and unloading up to 160 kN (P = 80 kN) load. Results based on the finite element model also show that at 163 kN (P = 81.5 kN), the mid-span deformation increases from 150 mm to 242.8 mm (a 3 kN increase in the total load causes a 90 mm increase in deformation). After unloading, the residual deformation is calculated as 178.3 mm compared to 184 mm measured using a string line, only 3% difference.

4.2.3 Discussions

During the test, measurements for deformation were made at various load steps and compared with results from the analytical solution to verify the accuracy of the bending operation before proceeding to higher loads. The various load steps of the bending operation from 0 to 157 kN (P = 78.5 kN) are shown in Table 3.

The plots in Fig. 11 show that the variation of the mid-span deformation with the applied loads is a straight line (elastic region) up to 100 kN (P = 50 kN). This corresponds to the load where yield initiates (f_y = 290.7 MPa) at the tip of the flange section. The yield load was calculated from the analytical solution as P_{yield} = 53.9 kN (Gergess and Sen 2016). At this load, testing was dwelled for 15 seconds to compare measured and calculated deformation. Results are shown in Table 4 (measured deformation of 41.3 mm compared to 39.2 mm from the analytical solution).

The loads were then increased to 150 kN (P = 75 kN) and dwelled for 29 seconds. Displacements were also compared with analytical results to ensure good correlation (83.2 mm measured deformation compared to 83 mm calculated). Finally, the loads were increased to 157 kN (P = 78.5 kN), dwelled for 60 seconds (119.4mm measured compared to 123.2 mm calculated) and then released to 0 kN (unloading).

It shall be noted that based on the analytical solution (Gergess and Sen 2016), the plastic load (load at which the section becomes fully plastic) was calculated as $P_{plastic}$ = 80.9 kN, slightly larger than the test load P = 78.5 kN in the first loading and slightly smaller than the test load P = 81.5 kN in the second loading.

In the second loading, loads were increased to 163 kN (P = 81.5 kN) after unloading from 157 kN (P = 78.5 kN) to 0. Loads were dwelled at 158 kN and 160 kN for few seconds before reaching the maximum load of 163 kN. Fig. 11 shows that for a 6 kN increase in the total load (from 157 kN to 163 kN), the maximum deformation increases from 119.4 mm to 242.8 mm (2 times larger) and the residual deformation after unloading increases from 56 mm (unloading from 157 kN) to 178.3 mm (unloading from 163 kN) (3 times larger). Fig. 11 shows that the mid-span deformation exhibits more or less a linear variation in the post-plastic range ($P > P_{\mathrm{plastic}}$ = 80.9 kN) and the rate of change of deformation versus load is 41 mm per kN. This confirms the sensitivity of deformations in the post-plastic range.

4.3 Effects of initial residual stress

In the initial finite element model, residual stresses that build up from fabrication of the straight girder were not included as no measurements were made to find out if they existed. Still, close correlation was noted in measured and calculated displacements during loading and unloading as shown in the previous section.

The effects of initial residual stress on the structural behavior of the steel girder during bending were considered in the finite element model for the first loading of 157 kN. As noted earlier, the imperfection amplitude of t_f/1000 was adopted as it gave the closest value of deformation (difference less than 1%). In absence of measured values, the predictive model of Salmon *et al*. (2010) for hot-rolled sections was adopted (shown in Fig. 8). Stresses in the flanges varied from 83 MPa in compression at the tip of the flange to about 70 MPa in tension at mid-width of the flange. In the web, initial residual stresses were in tension at the web-flange connection (around 50 MPa). At mid-web depth, stresses are in compression (approximately 50 MPa).

It is shown in Fig. 12 that initial residual stresses (Salmon *et al*. 2010) have an insignificant impact on deformations during loading (P = 78.5 kN) and unloading. Further investigations were conducted considering different patterns of initial residual stress to examine their impact on the girder response. These included increasing the magnitude of the initial residual stresses shown in Fig. 8 by up to 40% and/or changing the sign and pattern of the stresses. Comparisons of results in Table 5 show good correlation between the models with and without initial residual stresses. Table 5 shows that the difference between the maximum deformation at mid-span from the finite

Table 4 Test details for the first loading (load varies from 0 to 157 kN)

Command	Rate (mm/min)	Time (sec)		Load (kN)		Displacement (mm)		
		Start	End	Start	End	Start	End	Analytical
Go to 100 kN	14	0	167	0	100	0	41.3	39.2
Dwell 15 sec	-	167	182	100	98.9	41.3	41.3	39.2
Go to 150 kN	14	182	313	98.9	150	41.3	83.2	83
Dwell 29 sec	-	313	342	150	142.8	83.2	83.2	83
Go to 157 kN	6	342	658	142.8	157	83.2	119.4	123.2

Table 5 Comparison of mid-span displacements at P = 78.5 kN for various models without and with residual stress (RS) based on FEM with test results

Case	Test	W/O RS	With RS (Fig. 8)	With RS (10% ↑)	With RS (20% ↑)	With RS (40% ↑)	With RS (Opposite signs)	With RS (Different pattern)
δ_{max} (mm)	119.4	120.5	119.9	119.4	120.5	120.4	118.74	123
Difference		< 1%	< 1%	0%	< 1%	< 1%	< 1%	3%

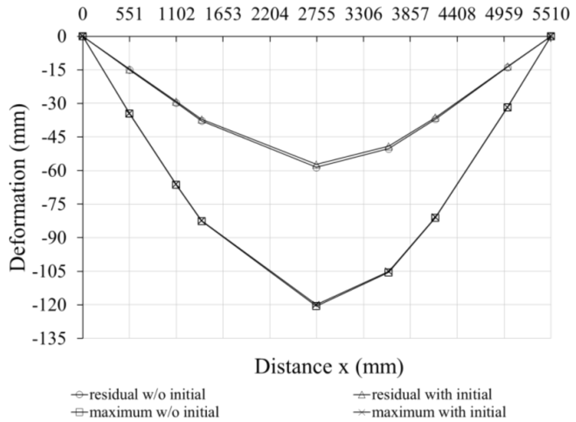

Fig. 12 Deformed shape considering initial residual stresses (Salmon *et al*. 2010) for the maximum load of 157 kN (P = 78.5 kN) based on FEM

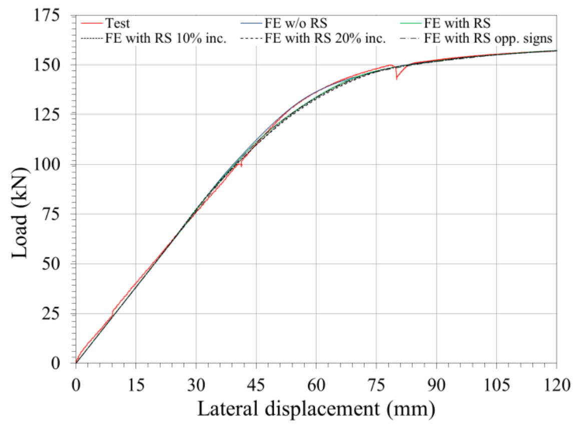

Fig. 13 Effect of initial residual stresses on deformation: load vs. lateral mid-span deflection (experimental and finite element analysis)

element model and the experimental results at P = 78.5 kN is less than 3% even if the magnitude of residual stresses is increased (up to 40%) and/or the pattern and sign of stresses are changed.

The load-displacement curve for the mid-span deformation from the experiment and the finite element analysis (without and without initial residual stresses) are shown in Fig. 13 during loading up to P = 78.5 kN. It can be concluded that the effect of the initial residual stresses on the cold bending operation displacement is not considerable.

4.4 Strains

As for deformation, strains were recorded during testing (loading and unloading) at small time intervals for P = 78.5 kN and P = 81.5 kN. These strains are compared with results from the finite element model. As noted earlier, strain gauges were placed at 44 different locations (Table 1). However, final measurements at maximum loads were only possible at 16 locations (the maximum number of channels that the data acquisitions system FDS DAQ can accommodate). These included critical points at mid-span (labelled D), at load points (labelled C), at the onset of yield points (labelled B) as well other locations arbitrarily selected between load points (labelled E) in the elastic region (labelled A) and inelastic region (labelled F). These locations are shown in Table 1.

Strain variations based on finite element modelling (FEM) with and without initial residual stresses are presented in Fig. 14 and are compared with measured values. These are strains due to bending measured along the longitudinal axis of the steel girder (z direction, Fig. 6). Note that initial residual stresses are based on Fig. 8 only as the variations considered in the previous section did not affect the results. Strain variations are shown at three critical locations: (a) D1FF, maximum compression strain at mid-span at 1cm from the flange tip; (b) D2BFI, maximum compression strain at mid-span at 5 cm from the flange tip; and (c) D4BFO, maximum tension strain at mid-span at 1.7 cm from the bottom flange tip. It is shown that up to the load of 157 kN, compression strains (D1FF and D2BFI) are comparable during loading and unloading. For the 163 kN load, strains during loading are also comparable (mainly compression strain at D2BFI and tension strain at D4BF). Note that at 163 kN, strains were measured during loading only.

4.4.1 Discussion

Results of strains at 157 kN (P = 78.5 kN) and after unloading, are summarized in Table 6. Comparisons show good correlation for the compression strain at D1FF (Fig. 14(a)) with initial residual stress (ratio of strain from numerical analysis to measured value is 1.13) and without initial residual stress (ratio of strain from numerical analysis to measured value is 1.1). Close results are also noted at D2BFI as shown in Fig. 14(b) (ratio of strain from numerical analysis to measured value is 0.89 with initial residual stress and 0.93 without initial residual stress). On the tension side and during loading, the ratio of strain from numerical analysis to measured value is 1.27 (with initial residual stress) and 1.32 (without initial residual stress) based on readings from the strain gauges at D4BFO (Fig. 14(c)). During unloading from 157 kN to 0, the ratios increased to 1.81 and 1.89 respectively. Despite these large differences, the strain gauge at this location did perform normally during reloading to 163 kN (P = 81.5 kN). From

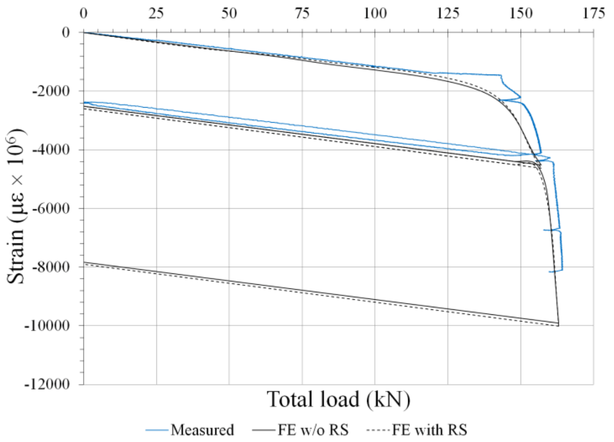

(a) Strain variation at mid-span at 1 cm from top of flange (D1FF)

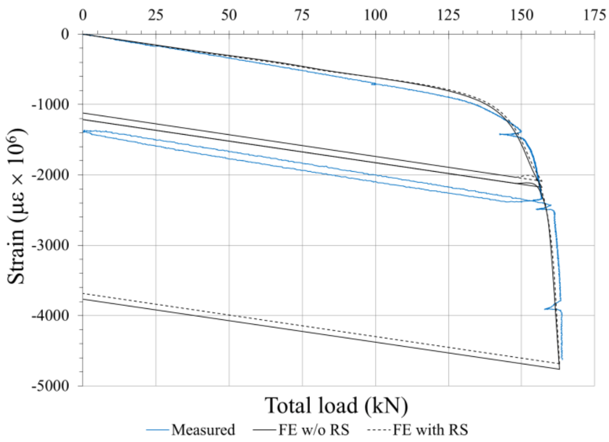

(b) Strain variation at mid-span at 5 cm from top of flange (D2BFI)

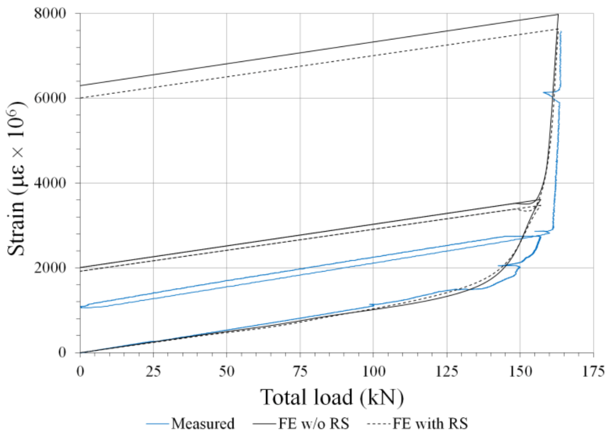

(c) Strain variation at mid-span at 1.7 cm from the tip of bottom flange (D4BFO)

Fig. 14 Strain variations during loading and unloading

Table 6 Strains during loading to 157 kN and unloading

Location	Measured ($\mu\varepsilon$)	FEM w/o RS $\mu\varepsilon$	FEM with RS $\mu\varepsilon$	FEM w/o RS/ Measured	FEM with RS/ Measured
DIFF loading	4,091 $\mu\varepsilon$ (2.96ε_y)	4,512 $\mu\varepsilon$ (3.26ε_y)	4,624 $\mu\varepsilon$ (3.34ε_y)	1.10	1.13
Unloading	2,374 $\mu\varepsilon$ (1.72ε_y)	2,512 $\mu\varepsilon$ (1.82ε_y)	2,595 $\mu\varepsilon$ (1.88ε_y)	1.06	1.09
D2BFI loading	2,337 $\mu\varepsilon$ (1.69ε_y)	2,176 $\mu\varepsilon$ (1.57ε_y)	2,089 $\mu\varepsilon$ (1.51ε_y)	0.93	0.89
Unloading	1,369 $\mu\varepsilon$ (0.99ε_y)	1,212 $\mu\varepsilon$ (0.88ε_y)	1,120 $\mu\varepsilon$ (0.81ε_y)	0.89	0.82
D4BFO* loading	2,732 $\mu\varepsilon$ (1.97ε_y)	3,612 $\mu\varepsilon$ (2.61ε_y)	3,475 $\mu\varepsilon$ (2.51ε_y)	1.32	1.27
Unloading	1,061 $\mu\varepsilon$ (0.77ε_y)	2,010 $\mu\varepsilon$ (1.45ε_y)	1,922 $\mu\varepsilon$ (1.39ε_y)	1.89	1.81

*Strain gauge performed normally during the second loading (Table 7)

Table 7 Strains during loading to 163kN and unloading

Location	Measured ($\mu\varepsilon$)	FEM w/o RS $\mu\varepsilon$	FEM with RS $\mu\varepsilon$	FEM w/o RS/ Measured	FEM with RS/ Measured
DIFF loading	8,159 $\mu\varepsilon$ (5.90ε_y)	9,907 $\mu\varepsilon$ (7.16ε_y)	10,010 $\mu\varepsilon$ (7.23ε_y)	1.21	1.22
Unloading	Not measured	7,830 $\mu\varepsilon$ (5.66ε_y)	7,901 $\mu\varepsilon$ (5.71ε_y)	-	-
D2BFI loading	4,625 $\mu\varepsilon$ (3.34ε_y)	4,762 $\mu\varepsilon$ (3.44ε_y)	4,684 $\mu\varepsilon$ (3.38ε_y)	1.03	1.01
Unloading	Not measured	3,766 $\mu\varepsilon$ (2.72ε_y)	3,685 $\mu\varepsilon$ (2.66ε_y)	-	-
D4BFO* loading	7,583 $\mu\varepsilon$ (5.48ε_y)	7,978 $\mu\varepsilon$ (5.76ε_y)	7,635 $\mu\varepsilon$ (5.52ε_y)	1.05	1.01
Unloading	Not measured	6,298 $\mu\varepsilon$ (4.55ε_y)	6,007 $\mu\varepsilon$ (4.34ε_y)	-	-

Table 7, the ratio of strain from numerical analysis to measured value is 1.01 (with initial residual stress) and 1.05 (without initial residual stress). Measurements were not available after unloading and therefore only calculated values with and without initial residual stress are presented in Table 7.

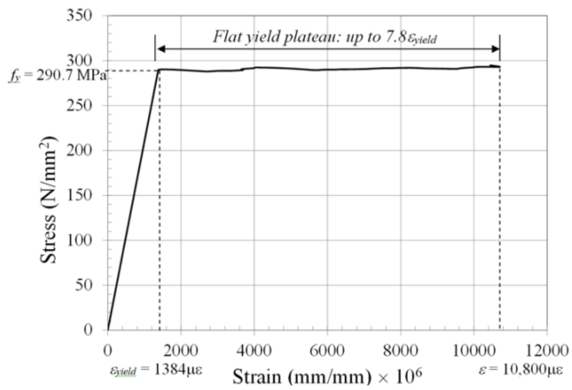

Fig. 15 Stress-strain curve flat yield plateau

In summary, strain readings do confirm the validity of the finite element analysis (as in deformations). The maximum strain is noted at D1FF equal to 10,010 $\mu\varepsilon \approx 7.23\varepsilon_{\text{yield}}$ at 1 cm from the flange tip. If this strain is extrapolated to the tip of the flange it becomes equal to 10,010 $\mu\varepsilon$ × (22 cm / 2) / 10 cm = 11,010 $\mu\varepsilon \approx 8.1\varepsilon_{\text{yield}}$, slightly exceeding the strain that corresponds to the end of the flat yield plateau of the stress-strain curve of 10,800 $\mu\varepsilon \approx 7.8\varepsilon_{\text{yield}}$ (Fig. 15). Note that the flat yield plateau for such conventional steel grade is usually set at 10 to 20ε_{yield} (Salmon *et al*. 2010). In all other cases, the maximum strain can be considered to fall within the yield plateau of the stress-strain curve and therefore Bauschinger effects (Bruneau *et al*. 1998, Hassan *et al*. 2018) (i.e., loss of isotropic behavior due to deformation produced in metallic materials) did not have to be considered. This ensures that the yield stress in tension and compression remain the same after bending.

4.5 Stress

In absence of measured stresses, stress diagrams obtained from the finite element analysis are shown during loading and unloading for the 157 kN and 163 kN loads. Stress diagrams are shown in Figs. 16 and 17 at mid-span with and without initial residual stress (critical section between load points that correspond to the maximum bending moment location). To show the impact of initial residual stress from fabrication on the cold bending residual stress, three cases were considered: (a) initial residual stress diagrams from Fig. 8 (Salmon *et al*. 2010); (b) initial residual stress diagrams from Fig. 8 increased by 20%; and (c) initial residual stress diagrams from Fig. 8 with the same magnitude but reversed in signs (although this case applies for built-up sections, it is considered for comparison purposes).

4.5.1 Stress at 157 kN (P = 78.5 kN) and after unloading

During loading, the flange exhibits an elasto-plastic (almost fully plastic) behavior as shown in Fig. 16(a). This is due to the fact that the point load P = 78.5 kN is almost equal to the plastic load P_{plastic} = 80.9 kN determined from the analytical solution (Section 4.5.3). Initial residual stress did not affect the stress diagrams at maximum loads as shown in Fig. 16(a).

In the web, stresses were much smaller. For P = 78.5 kN, in absence of initial residual stresses, the stress at the mid-web height is 3.8 MPa (in compression). This value increases to 8.6 MPa if initial residual stresses are considered (based on Fig. 8) and reaches a maximum of 10 MPa when the magnitude of the initial residual stresses is increased by 20%. Finally, when the initial residual stresses are reversed the stress becomes tensile with a magnitude of approximately 1 MPa (Fig. 16(a)).

After unloading residual stresses in the flanges and web are shown in Fig. 16(b). They vary from 100 MPa at the flange tip to 115 MPa close to the web without considering initial residual stresses. If residual stresses were considered (based on Fig. 8, increased by 20% and signs reversed), the residual stress at the flange tip remains the same (100 MPa). Contrarily, the variation is noticeable close to the web as the stress increases from 115 MPa without initial stress to 140 MPa based on the initial stress from Fig. 8, to 145 MPa based on the initial stress from Fig. 8 by 20% and it reduces to about 70 MPa for the initial residual stress diagrams from Fig. 8 reversed in sign.

In the web (Fig. 16(b)), the residual stress variation is insignificant. A stress value of 1.25 MPa (compression) is noted a mid-web depth if initial residual stresses are not considered. It increases to 4.4 MPa if residual stresses are considered (Fig. 8), to 5.4 MPa if initial stresses are increased by 20% and becomes tensile (1.8 MPa) if the signs of initial stresses are reversed.

Note in all cases that stress distributions in the two sides of the flanges are equal but reversed in sign. This zigzag distribution of residual stress through the flange width after the girder is unloaded (Fig. 16(b)) is common for structural steel members, with the magnitude of the residual stresses dependent on the bending loads (Keating and Christian 2009).

4.5.2 Stress at 163 kN (P = 81.5 kN) and after unloading

Residual stresses after unloading from 157 kN to 0 (Fig. 16(b)) constitute the initial conditions for the section during bending at 163 kN. As in the previous case, the flanges exhibit an almost fully plastic behavior (Fig. 17(a)) at 163 kN. Slight variations are noted in the web but still insignificant (the maximum value in compression is around 9 MPa at mid-web height and did not change much if initial stresses are considered). If initial stresses are reversed in sign, the maximum stress becomes compressive at mid-height of the web (around 5.8 MPa compare to a tensile stress of almost 1 MPa at 157 kN).

After unloading, residual stress diagrams in the flange and web are shown in Fig. 17(b). At the flange tip, the residual stress is 115 MPa at 163 kN (compared to 100 MPa at 157 kN). Similar values are noted with and without initial stress.

Close to the web, the residual stress is equal to 130MPa at 163 kN (compared to 115 MPa at 157 kN) without considering initial residual stress. If initial residual stresses are considered, the stress is equal to 145 MPa (same value for initial residual stress diagrams from Fig. 8 and for the case where they are increased by 20%). It reduces to about

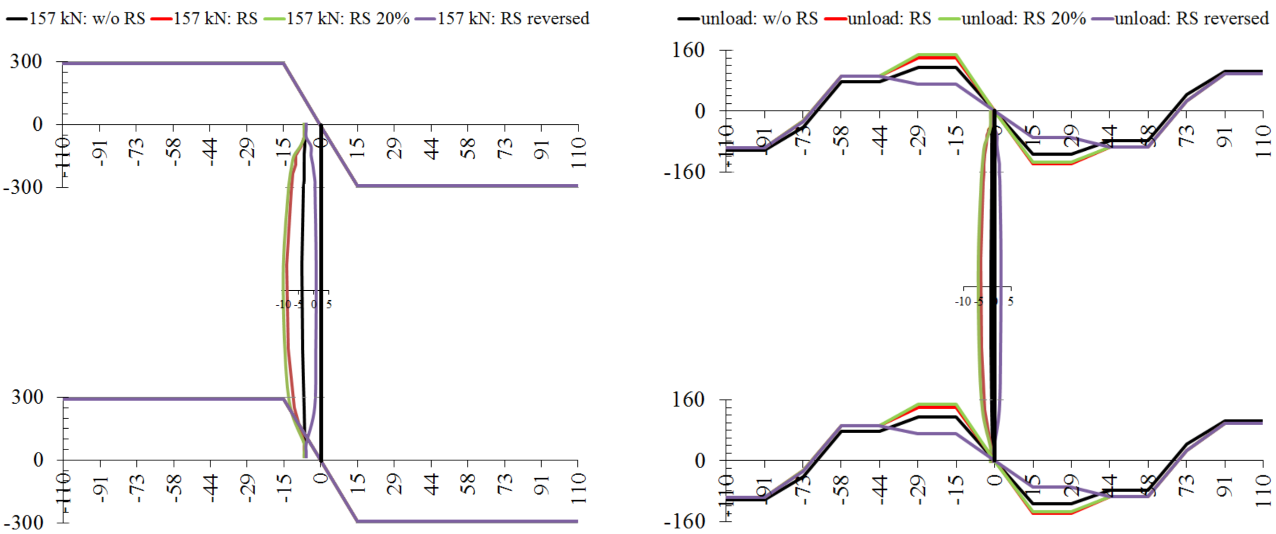

(a) Loading to 157 kN (b) Unloading

Fig. 16 Stress diagrams: first loading (157 kN) (*Note: Vertical axis limits vary between Figs. 16(a) and (b))

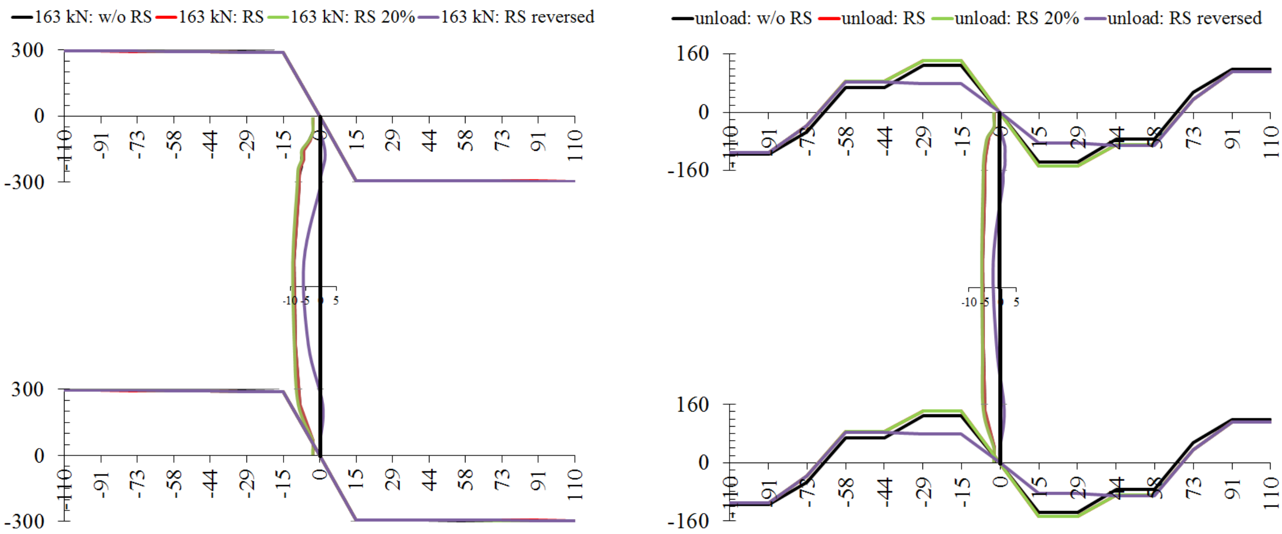

(a) Loading to 163 kN (b) Unloading

Fig. 17 Stress diagrams: second loading (163 kN) (*Note: Vertical axis limits vary between Figs. 17(a) and (b))

80 MPa if the initial residual stress values from Fig. 8 are reversed in sign.

In the web (Fig. 17(b)), residual stresses are insignificant as in the previous case. A maximum value of 5.4 MPa is noted a mid-web depth if initial residual stresses are not considered.

4.5.3 Discussions

Residual stresses that build up in the steel section after unloading are critical. The maximum values noted at the flange tips (100 MPa for the 157 kN load case and 115 MPa for the 163 kN load case) correspond to $0.34f_y$ and $0.4f_y$ respectively. These stresses are tensile at one side of the flange and compressive at the other side. Consequently, they may affect the steel section under service loads (bent about its strong axis) as resulting stresses in the flange will be in compression or tension depending on the sign of the bending moment. Residual stresses are even larger along the flange section close to the web (≈ 145 MPa) equivalent to about $0.5f_y$, a critical value for the 157 kN and 163 kN cases if initial residual stresses are increased by 20%. In the web, residual stresses due to bending are inconsiderable (expected as the girder is bent about its weak axis).

In summary, cold bending induces residual stresses of considerable magnitude, irrespective of the initial residual stress values and distribution. Residual stresses can reduce the apparent stiffness of the material, as yielding occurs at lower stress levels upon loading the curved beam about its strong axis (Keating and Christian 2009). According to AASHTO (2014), residual stress effects due to cold bending and/or cooling after rolling or welding are equivalent to $0.3f_y$ (yield strength reduced by 30%). In a previous AASHTO edition (2004), the compression flange stress at the onset of nominal yielding was set at $0.5f_y$ (e.g., residual stresses were considered equal to $0.5f_y$) to avoid anomalous situations for some types of cross-sections. Consequently, in this paper it is recommended to set the stress in the flanges at the onset of nominal yielding equal to $0.5f_y$ for steel girders curved by four-point bending.

It shall be noted that the effect of residual stress from cold bending on the service load capacity and fatigue load resistance of the steel section in service is being investigated theoretically and experimentally and results will be published soon.

5. Conclusions

This paper provides an analytical and experimental investigation of rolled steel sections curved by the point bending method. It determines the structural response of the steel section during bending in the elasto-plastic and post-plastic ranges. A full-scale test was performed considering a full-size steel rolled shape (IPE600 European section) that was subjected to two loadings: (1) an elasto-plastic load of 157 kN; and (2) a post-plastic load to 163 kN. Deformation and strain were recorded at different load increments using LDVTs and strain gauges. These measurements were compared with results from a non-linear three-dimensional (3D) finite element analysis using the finite element package ABAQUS.

The finite element model was first validated based on induced deformations. Good correlation was noted between measured and calculated values (within 1% in the elasto-plastic range and 3 to 8% in the post-plastic range). Initial residual stresses, geometric non-linearity and imperfections were also considered in the finite element analysis based on available predictive models. It was shown that they did not affect the girder geometric behaviour as induced deformations were almost invariant.

Plots of the strain variation with the applied load were then provided for the purpose of comparisons between measured and calculated values. Predicted values were in reasonable agreement with test results (1 to 20% depending on the strain gauge location and loading). As for deformations, initial stresses and geometric imperfections did not affect the strain variation. It shall be noted that the maximum strain at the post-plastic load of 163 kN was within the flat yield plateau of the stress-strain curve.

The validated finite element model was finally used to calculate stresses at critical locations (point of maximum moment between point loads) during loading and unloading (in absence of measured data). The analysis showed that the stress distribution across the flange cross-section was fully plastic at the maximum loads and that the residual stress after unloading varied from $0.34f_y$ to $0.4f_y$ at the flange tip and $0.4f_y$ and $0.45f_y$ close to the web. It was also shown that initial residual stress from fabrication did not affect the residual stresses due to cold bending at the flange tip but increased the stress close to the web to $0.5f_y$. Stresses in the web were of low magnitude (< 10 MPa). A recommendation was finally made to set the stress in the flanges at the onset of nominal yielding equal to $0.5f_y$ for steel girders curved by cold bending.

This paper sets up basis for more rigorous research (currently being conducted for steel rolled shapes of various length and size) for investigating the effects of cold curving on the service load capacity and fatigue load resistance of hot-rolled steel girders in service.

Acknowledgments

The authors are indebted to ECM Lebanon and YLE Engineering for their valuable assistance in the experimental work. They are also grateful to Mrs. Nina Helal and Dr. Jihad Rishmani at the University of Balamand.

References

AASHTO (2004), AASHTO LRFD bridge design specifications, (3rd Edition), Published by the American Association of State Highway & Transportation Officials, Washington, DC, USA.

AASHTO (2014), AASHTO LRFD bridge design specifications, (7th Edition), Published by the American Association of State Highway & Transportation Officials, Washington, DC, USA.

Abambres, M. and Quach, W. (2014), "Residual Stresses in steel members: a review of available analytical expressions", *Int. J. Struct. Integrity*, **7**(1), 70-94.

ANSI/AISC 360-10 (2015), Specification for structural steel buildings, (4th Printing), American Institute of Steel Construction, Chicago, IL, USA.

ASTM (2014), Standard test methods for tension testing of metallic materials, ASTM Designation: E8/E8M - 13a, AASHTO No. T68, an American National Standard, USA.

Bruneau, M., Uang, C. and Whittaker, A. (1998), *Ductile Design of Steel Structures*, McGraw-Hill, New York, NY, USA.

BSK 99 (2003), Swedish design rules for steel structures, Boverket, Karlskrona, Sweden.

Chen, Y., Chen, X. and Wang, C. (2016), "Tests and behavior of hot-rolled channel steel sections subjected to web crippling", *J. Constr. Steel Res.*, **117**, 101-114.

Dawson, R.G. and Walker, A.C. (1972), "Post-buckling of geometrically imperfect plates", *J. Struct. Div., ASCE*, **98**(1), 75-94.

European Convention for Constructional Steelwork (ECCS), (1984), Ultimate limit state calculation of sway frames with rigid joints; Technical Committee 8 - Structural Stability Technical Working Group 8.2, Publication No. 33, Paris, France.

Gergess, A. and Sen, R. (2010), "Post-yield response of cold-cambered wide-flange steel beams", *J. Constr. Steel Res.*, **66**, 1155-1163.

Gergess, A. and Sen, R. (2016), "Curving structural steel girders by two-point bending", *J. Constr. Steel Res.*, **122**, 511-519.

Hassan, M.S., Salawdeh, S. and Goggins, J. (2018), "Determination of geometrical imperfection models in finite element analysis of structural steel hollow sections under cyclic axial loading", *J. Constr. Steel Res.*, **141**, 189-203.

Hibbitt, Karlsson and Sorensen, Inc. (2012), ABAQUS/Standard User's Manual Volumes I-III and Abaqus CAE Manual; Version 6.12, Pawtucket, RI, USA.

Keating, P.B. and Christian, L.C. (2009), "Effetcs of bending and heat on the ductility and fracture toughness of flange plate", Report No. 0-4624-2; Texas Department of Transportation, Austin, TX, USA.

Lay, M.G. and Ward, R. (1969), "Residual stresses in steel sections", *J. Austral. Inst. Steel Constr.*, **33**, 2-21.

Liu, W., Rasmussen, K.J.R. and Zhang, H. (2017), "Modelling and

probabilistic study of the residual stress of cold-formed hollow steel sections", *Eng. Struct.*, **150**, 986-995.
Madugula, M.K.S., Haidur, R., Monforton, G.R. and Marshall, D.G. (1997), "Additional residual stress and yield stress tests on hot-rolled angle", *Proceedings of the Structural Stability Research Council Annual Technical Session*, Toronto, Canada.
Nethercot, D.A. (1974), "Residual stresses and their influence upon the lateral buckling of rolled steel beams", *J. Inst. Struct. Engr.*, **352**, 89-96.
Reis, A., Lopes, N., Real, E. and Real, P.V. (2016), "Numerical modelling of steel plate girders at normal and elevated temperatures", *Fire Safety J.*, **86**, 1-15.
Saliba, N. and Gardner, L. (2013), "Cross-section stability of lean duplex stainless steel welded I-sections", *J. Constr. Steel Res.*, **80**, 1-14.
Salmon, C.G., Malhas, F.A. and Johnson, J.E. (2010), *Steel Structures: Design and Behavior*, (5th Edition), Harper-Collins, NY, USA.
Sonck, D. and Belis, J. (2016), "Weak-axis flecural buckling of cellular and castellated columns", *J. Constr. Steel Res.*, **124**, 91-100.
Szalai, J. and Papp, F. (2005), "A new residual stress distribution for hot-rolled I shaped sections", *J. Constr. Steel Res.*, **61**(6), 845-861.
Thombare, C.N., Sangle, K.K. and Mohitkar, V.M. (2016), "Nonlinear buckling analysis of 2-D cold-formed steel simple cross-aisle storage rack frames", *J. Build. Eng.*, **7**, 12-22.
Trahair, N.S. (1993), *Flexural-Torsional Buckling of Structures*, E & FN Spon, London, UK.
Wang, J., Afshan, S. and Gardner, L. (2017), "Axial behaviour of prestressed high strength steel tubular members", *J. Constr. Steel Res.*, **133**, 547-563.
Wang, J., Afshan, S., Gkantou, M., Theofanous, M., Baniotopoulos, C. and Gardner, L. (2016), "Flexural behaviour of hot-finished high strength steel square and rectangular hollow sections", *J. Constr. Steel Res.*, **121**, 97-109.
Young, B.W. (1972), "Residual stresses in hot-rolled members", *Proceedings of the IABSE International Colloquium on Column Strength*, Paris, France.
Yun, X., Gardner, L. and Boissonnade, N. (2018), "The continuous strength method for the design of hot-rolled steel cross-sections", *Eng. Struct.*, **157**, 179-191.

DL

Nomenclature

a'	offset of point load from end supports
b	overhang dimension
b_f	flange width
d	girder depth
$\boldsymbol{E}$	**modulus of elasticity**
f_y	**yield stress**
f_u	ultimate tensile **stress**
$\boldsymbol{L}$	girder length between end supports
$\boldsymbol{L'}$	total girder **length**
$\boldsymbol{P}$	point **load** magnitude
$\boldsymbol{P}_{yield}$	yield point **load** magnitude
$\boldsymbol{P}_{plastic}$	plastic point **load** magnitude
$\boldsymbol{t_f}$	**flange thickness**
$\boldsymbol{t_w}$	**web thickness**
x	lateral offset
y	vertical offset from top flange
z	offset along girder length
γ	coefficient for imperfection amplitude
ε	residual strain
ε_y	yield strain
$\delta_{\max}$	maximum midspan displacement
σ_{cr}	elastic critical buckling stress
ω	imperfection amplitude